PCCP

PAPER

View Article Online
View Journal | View Issue

Cite this: *Phys. Chem. Chem. Phys.*, 2026, **28**, 7521

Microscopic visualization of $NiFeO_x$ and NiO_x cocatalyst effects on charge carrier dynamics of $BiVO_4$ photoanodes

Yuki Nakatsukasa, Haruka Nobuoka and Kenji Katayama *

Improving the interfacial charge carrier dynamics of $BiVO_4$ photoanodes is essential for achieving higher efficiency in photoelectrochemical water oxidation. In this study, we investigated the effects of $NiFeO_x$ and NiO_x cocatalysts on $BiVO_4$ by combining patterned-illumination time-resolved phase microscopy (PI-PM) and photoelectrochemical measurements, including impedance spectroscopy. Both cocatalysts substantially enhance the photocurrent and charge-injection efficiency (η_{inj}), whereas the bulk charge-separation efficiency (η_{sep}) remains less changed (within ±6%), indicating that the improvements originate from the interfacial hole transfer process. PI-PM visualizes the local trapped-carrier dynamics and reveals the differences in trapped-carrier activity between the cocatalysts. $NiFeO_x$ introduces spatially localized slow-decay hole and electron components that correspond to reactive carrier populations, while NiO_x generates a more uniform distribution of reactive domains with increased spatial coverage and prolonged carrier lifetimes. These microscopic differences correlate with macroscopic performance, with NiO_x achieving the highest η_{inj} and photocurrent (1.98 mA cm^{-2}). The combined results demonstrate that $NiFeO_x$ locally enhances the catalytic activity at selective surface regions, whereas NiO_x promotes more homogeneous interfacial charge extraction across the $BiVO_4$ surface.

Received 27th December 2025,
Accepted 18th February 2026

DOI: 10.1039/d5cp05032d

rsc.li/pccp

Introduction

Bismuth vanadate ($BiVO_4$) has been widely recognized as one of the most promising visible-light-responsive photocatalysts for oxygen evolution because of its suitable band gap (~2.4 eV), relatively high chemical stability, and compatibility with various fabrication methods. Owing to these characteristics, $BiVO_4$ has been extensively investigated for photocatalytic and photoelectrochemical water oxidation,[1–8] where the overall performance is strongly governed by the generation, separation, and interfacial utilization of photogenerated charge carriers. Despite these advantages, the photocurrent and quantum efficiency of $BiVO_4$-based systems remain significantly lower than the theoretical values due to carrier recombination, defect states and sluggish surface water-oxidation kinetics.

Loading cocatalysts onto semiconductor surfaces is one of the most effective routes to improve photocatalytic and PEC performance. Cocatalysts generally accelerate interfacial charge transfer, suppress surface recombination, and modify local energetics to facilitate desired redox reactions.[9] Among various candidates, $NiFeO_x$ and NiO_x have attracted particular attention as oxygen-evolution cocatalysts (OECs) due to their earth-abundant composition and high intrinsic activity. $NiFeO_x$ has been widely used to improve PEC water oxidation, offering advantages such as enhanced hole accumulation and reduced surface recombination.[10–14] In contrast, NiO_x, although less explored, possesses distinct catalytic and electronic properties, such as p-type conductivity and favorable band alignment with $BiVO_4$ that may lead to different pathways for charge accumulation, defect passivation, and carrier stabilization.[15–18]

Understanding the enhancement mechanisms provided by these cocatalysts requires direct observation of the underlying charge carrier dynamics. Such dynamics offer fundamental insight into how cocatalysts modify trapping, recombination, and interfacial transfer processes. From this perspective, in general, transient absorption (TA) spectroscopy[19–22] and time-resolved photoluminescence (TRPL)[23] have been employed to study carrier behavior in $BiVO_4$. The cocatalyst-induced longer lifetime of charge carriers has been studied by monitoring appropriate probe wavelengths.[24] These methods have been mainly used for monitoring the free charge carriers in the conduction and valence bands.

As a complementary approach to TA and TRPL, we have developed the patterned-illumination time-resolved phase microscopy (PI-PM) method,[25] which visualizes local trapped-carrier (not free charge-carrier) dynamics through refractive index changes with microscopic spatial resolution, caused by

Department of Applied Chemistry, Chuo University, Tokyo 112-8551, Japan.
E-mail: kkata.33g@g.chuo-u.ac.jp; Tel: +81-3-3817-1913

charge accumulation at the interface. This technique has revealed key aspects of charge trapping, interfacial reactions, and cocatalyst functions on various photocatalysts. Our previous studies demonstrated the local charge carrier dynamics of $BiVO_4$ prepared by different synthetic methods,[26] as well as provided microscopic insight into cocatalyst-related processes such as CoO_x and Rh on $BiVO_4$.[27,28] These reports highlight the utility of PI-PM in distinguishing electron and hole contributions, identifying reactive *versus* nonreactive trap states, and mapping heterogeneous surface activity.

In this study, we apply PI-PM to elucidate the effects of $NiFeO_x$ and NiO_x cocatalysts on $BiVO_4$ photoanodes. We found that NiO_x fabrication leads to a remarkably high photocurrent of 1.98 mA cm^{-2}, surpassing that of $NiFeO_x$-modified $BiVO_4$ under similar preparation conditions. By combining surface structural analysis, electrical characterization (PEIS), and microscopic charge-carrier imaging (PI-PM), we systematically investigate how these cocatalysts alter surface energetics and interfacial dynamics. Through this comprehensive approach, we clarify the origin of the superior performance of NiO_x. Although PI-PM has been previously employed to investigate charge-carrier dynamics in photocatalytic systems, a direct microscopic comparison of multiple high-performance cocatalysts under identical conditions has not yet been reported. In this work, we comparatively examine $NiFeO_x$ and NiO_x overlayers on $BiVO_4$ to elucidate how differences in the spatial distribution and lifetime of interfacial carriers translate into distinct charge-injection efficiencies and PEC performance. This comparative approach enables a mechanistic understanding of cocatalyst functionality at the microscopic level. To clarify the overall conceptual framework, a schematic illustration of the PI-PM methodology and its relation to photoelectrochemical (PEC) performance is presented in Fig. 1.

Experimental

PI-PM method

The PI-PM technique is a time-resolved pump–probe microscopy method that visualizes the dynamics of photo-excited charge carriers through refractive index variations detected by

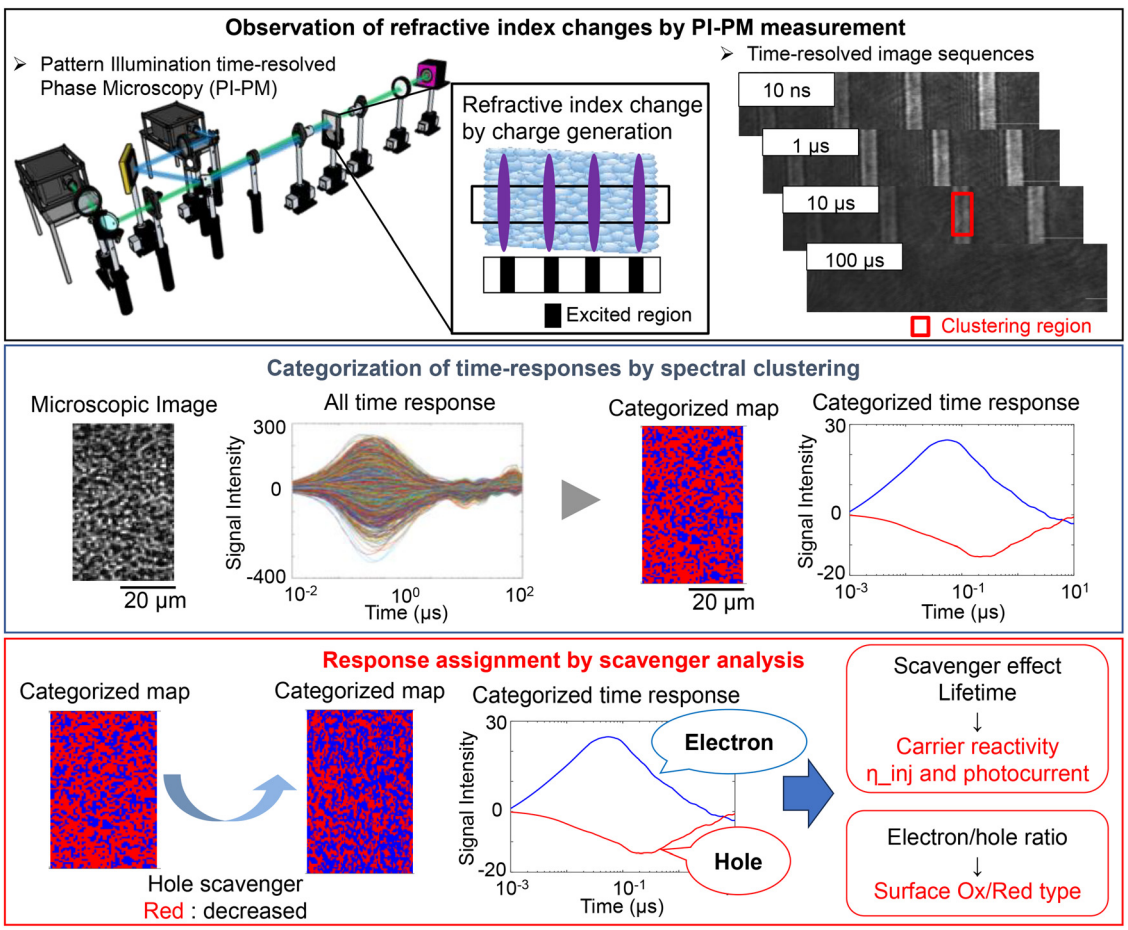

Fig. 1 Conceptual schematic of the PI-PM methodology and carrier-classification framework used in this study. Photoexcitation induces refractive index changes associated with charge-carrier generation, which are recorded as time-resolved image sequences. Pixel-wise temporal responses are categorized by spectral clustering to generate spatial maps of carrier dynamics. Scavenger-dependent measurements enable the assignment of electron and hole populations. The extracted lifetimes and spatial fractions of reactive carriers are quantitatively correlated with the interfacial charge-injection efficiency and overall photoelectrochemical performance.

phase-contrast imaging.[25] In this setup, both the pump and probe lights are collimated to illuminate the sample surface over a region approximately 0.5 mm in diameter. A slight defocus adjustment converts the refractive index modulation into measurable phase contrast as an intensity contrast,[29] allowing non-radiative processes such as charge trapping and interfacial transfer to be visualized as temporal image sequences. Both lights are nanosecond pulsed (3–4 ns), and time-resolved images are obtained by electronically controlling the delay between the two pulses.

An arbitrary illumination pattern, generated using a digital micromirror device (DMD), is used as the pump light to selectively excite charge carriers within the sample. Following excitation, these carriers undergo processes such as trapping, recombination, and interfacial transfer, resulting in time-dependent refractive index changes that reflect carrier generation and decay. The spatial distribution of these processes is reconstructed as a microscopic image sequence. Because refractive index detection is sensitive to interfacial non-radiative carrier dynamics, PI-PM can probe surface-trapped carriers that are not accessible *via* TA or TRPL. The sign of the refractive index changes and the response to scavenger species at the solution interface enable distinction between different carrier types on the surface.

Images obtained under pulsed-laser illumination inherently contain intensity fluctuations due to shot noise and optical inhomogeneity. Therefore, the acquired image sequences are reconstructed using three-dimensional total-variation (TV) regularization across the spatial (x, y) and temporal (t) dimensions,[30] which effectively suppresses noise while preserving the structural and kinetic information. Because this procedure requires image contrast between illuminated and non-illuminated regions, pattern illumination is essential for the analysis.

A schematic of the optical setup is shown in Fig. S1 of the SI. In this experiment, a horizontally striped light pattern was employed as the pump beam, and the central area of the field of view was analyzed (total image area $\approx$480.8 $\times$ 93.9 μm^2, 1024 $\times$ 200 pixels, and pixel width = 469 nm). The pump and probe lights were generated from the third and second harmonics of Nd:YAG pulse lasers (GAIA, Rayture Systems) with pulse widths of $\approx$3 ns and wavelengths of 355 nm and 532 nm, respectively. The irradiated pump area had a diameter of 0.5 mm, and the pulse energies were 0.8 mJ (pump) and 0.02 mJ (probe). The optical resolution of the system was 2–3 μm. Although both refractive index and absorption changes can contribute to the detected signal, the absorption change of $BiVO_4$ was negligible at the probe wavelength (532 nm), under our setup conditions (wide-field detection).[27]

Clustering analysis

In the PI-PM analysis, classification of the surface charge carrier types was performed using clustering analysis. A representative region ($\approx$30 $\times$ 50 μm) within the pump-illuminated area was selected for evaluation. The time-resolved PI-PM dataset contains pixel-wise temporal signals, yielding more than 10 000 individual response curves, each composed of 100–200 data points spanning time scales from nanoseconds to milliseconds.

To categorize these responses, spectral clustering—a statistical classification method based on vector similarity—was employed.[31] Each temporal response was treated as a numerical vector, and the similarity between all vectors was quantified using a normalized correlation matrix. The clustering algorithm then grouped the signals exhibiting similar temporal behaviors into distinct categories that reflect different charge carrier dynamics.

Clustering analysis was performed automatically for all pixel-wise temporal responses. Pixels exhibiting extremely low signal intensity, corresponding to noise-dominated or no-response regions, were categorized as outliers based on a predefined signal threshold rather than kinetic features. The fraction of these low-signal responses is summarized in the tables accompanying each PI-PM figure. Finally, the classified responses were spatially mapped onto the corresponding optical image, allowing visualization of the spatial distribution of different charge carrier types and identification of their localized behaviors within the photo-excited region.

Sign of refractive index change

When the probe wavelength (532 nm) lies above the material's bandgap absorption edge, the contribution from optical absorption is negligible. Under such conditions, the PI-PM method predominantly detects refractive index changes that arise from trapped charge carriers at interfaces rather than from electronic transitions.[25] The accumulation of charges at an interface generates a local electric field, E_{local}, which can be expressed as:

$$E_{\mathrm{local}} = \frac{\sigma}{\varepsilon_{\mathrm{r}}\varepsilon_0}, \tag{1}$$

where σ is the surface charge density (positive for holes and negative for electrons), ε_{r} is the relative permittivity of the material, and ε_{r} is the vacuum permittivity. The direction of E_{local} depends on the sign of the accumulated charge carriers. This local electric field modulates the material's permittivity ε through the linear electro-optic (Pockels) effect:

$$\Delta\varepsilon = \varepsilon_{\mathrm{r}}{}^2 r E_{\mathrm{local}} \tag{2}$$

where r is the Pockels coefficient. For hole accumulation ($\sigma > 0$), the permittivity increases, whereas for electron accumulation ($\sigma < 0$), it decreases. Physically, electrons generate an inward electric field that reduces permittivity, resulting in a phase advance of the transmitted probe light, while holes induce the opposite effect. The corresponding change in refractive index, Δn, can be approximated by:

$$\Delta n \cong \frac{\Delta\varepsilon}{2n} \tag{3}$$

which follows from the first-order expansion of $(n + \Delta n)^2 \approx \varepsilon + \Delta\varepsilon$ under the assumption of small perturbations. Consequently, photo-excited electrons and holes produce refractive index

changes of opposite sign within the same dielectric medium. This polarity contrast enables the direct identification of carrier types in PI-PM imaging—responses with opposite phase shifts can be attributed to electrons and holes, respectively.

Sample preparation

Fabrication of $BiVO_4$ by metal–organic decomposition (MOD). $BiVO_4$ thin films were fabricated by the general metal–organic decomposition (MOD) method.[32–35] First, 3 mL of 0.2 M bismuth nitrate pentahydrate ($Bi(NO_3)_3{\cdot}5H_2O$) in acetic acid and 20 mL of 0.03 M vanadyl acetylacetonate [$VO(acac)_2$] in acetylacetone were prepared. The two precursor solutions were mixed and stirred for 30 min to obtain a homogeneous MOD precursor solution. This solution was spin-coated onto fluorine-doped tin oxide (FTO) glass substrates, followed by calcination at 450 °C for 1 h in air. The coating and calcination processes were repeated 15 times to achieve a sufficient film thickness. Finally, the resulting films were annealed at 450 °C for 10 h to obtain crystalline $BiVO_4$ photoanodes.

NiO_x modification. NiO_x layers were deposited onto the prepared $BiVO_4$ films by spin-coating a methanolic solution of 650 mM nickel(II) sulfate hexahydrate ($NiSO_4{\cdot}6H_2O$). The coated samples were then calcined at 450 °C for 2.5 h in air to form NiO_x-modified $BiVO_4$ electrodes.

$NiFeO_x$ cocatalyst loading. For the $NiFeO_x$-modified $BiVO_4$ samples, 5 mL of 650 mM $NiSO_4{\cdot}6H_2O$ in methanol and 5 mL of 150 mM iron(III) chloride hexahydrate ($FeCl_3{\cdot}6H_2O$) in methanol were prepared separately, then mixed and stirred for 30 min to yield a uniform precursor solution. The mixture was spin-coated onto the $BiVO_4$ films and subsequently calcined at 450 °C for 2.5 h in air. For the fabrication of NiO_x and $NiFeO_x$ modifications, we searched the optimal preparation conditions by modifying the concentration and calcination temperature to provide the best activity.

Measurement cell. The obtained $BiVO_4$-based film deposited on an FTO glass substrate was sealed with another glass substrate using a rubber spacer (thickness: 0.5 mm) to form a liquid cell. Approximately 0.15 mL of liquid was introduced into the interstitial gap. The measurements were conducted with acetonitrile (ACN), ethanol (EtOH), and a 0.1 mM nitrobenzene solution in EtOH (NB/EtOH) as contact solutions. ACN served as an inert solvent to suppress interfacial charge transfer between the photocatalyst and the liquid phase, whereas EtOH acted as a hole scavenger. The NB/EtOH solution functioned as a scavenger for both electrons and holes. In previous studies,[36] it was demonstrated that NB is reduced to nitrosobenzene during the photocatalytic reaction in EtOH, meaning that it works as an electron acceptor.

Photoelectrochemical (PEC) measurement. The photoelectrochemical performance of the $BiVO_4$-based electrodes was evaluated through photocurrent–voltage (J–V) measurements using a three-electrode PEC cell. The working electrode ($BiVO_4$-based sample) was illuminated through a circular aperture (diameter: 10 mm) under simulated solar light (AM 1.5G, 100 mW cm^{-2}, $\lambda > 420$ nm). A platinum wire and an Ag/AgCl electrode served as the counter and reference electrodes, respectively. The electrolyte consisted of a 0.1 M phosphate buffer solution (pH = 7.2). The applied potential was controlled using a potentiostat, and the J–V curves were recorded at a scan rate of 20 mV s^{-1} over a potential range from –0.6 to 0.6 V *vs.* Ag/AgCl. The charge separation (η_{sep}) and charge injection (η_{inj}) efficiencies were evaluated using the following relationships:

$$\eta_{sep} = \frac{J_{Na_2SO_3}}{J_{max}} \quad (4)$$

$$\eta_{inj} = \frac{J_{H_2O}}{J_{Na_2SO_3}} \quad (5)$$

where J_{H_2O} and $J_{Na_2SO_3}$ are the photocurrent densities measured in 0.1 M phosphate buffer solution and in 0.1 M Na_2SO_3 aqueous solution, respectively, and J_{max} (7.5 mA cm^{-2} for $BiVO_4$) represents the theoretical maximum photocurrent density. Here, η_{sep} denotes the efficiency of charge carrier separation (*i.e.*, carriers avoiding recombination), while η_{inj} represents the efficiency of interfacial hole transfer. In the Na_2SO_3 electrolyte, hole transfer is assumed to proceed as η_{inj} = 100%.

Photoelectrochemical impedance spectroscopy (PEIS). Electrochemical impedance spectroscopy (EIS) measurements were performed under illumination to evaluate the interfacial charge-transfer properties of the $BiVO_4$-based photoanodes. The measurements were conducted in a standard three-electrode configuration using a potentiostat (SI1287, Solatron), where the $BiVO_4$ sample served as the working electrode, a platinum wire as the counter electrode, and an Ag/AgCl (in saturated KCl) electrode as the reference. The potential values were converted to the reversible hydrogen electrode (RHE) scale. The electrolyte consisted of a 0.1 M phosphate buffer solution (PBS, pH 7.2). The impedance spectra were collected over the frequency range of 0.1 Hz–100 kHz with an AC amplitude of 5 mV at 1.23 V under AM 1.5 G illumination (100 mW cm^{-2}). The Nyquist plots were analyzed using equivalent circuit models fitted to extract the electrical parameters of the equivalent circuit model described in the text.

Other analysis methods. The surface morphology and microstructural features of the samples were examined using scanning electron microscopy (SEM, JSM7500FA, JEOL). The SEM images were acquired to evaluate the particle shape, size distribution, and surface roughness. Elemental compositions were analyzed by energy-dispersive X-ray spectroscopy (EDX, JSM7800F, JEOL). The EDX measurements provided spatially resolved information on the distribution of the constituent elements to confirm the loading of cocatalysts and the uniformity of the elemental composition.

Results and discussion

Fig. 1 shows the SEM images of (a) bare $BiVO_4$, (b) $BiVO_4$/$NiFeO_x$, and (c and d) $BiVO_4$/NiO_x photoanodes. The bare $BiVO_4$ film exhibits a homogeneous surface morphology composed of densely packed, particle-like domains with an average diameter of approximately 0.1–0.2 μm. Such a granular surface is typical

of $BiVO_4$ films prepared by the MOD method[32–35] and ensures sufficient surface area for subsequent co-catalyst deposition.

Upon the introduction of $NiFeO_x$, the overall surface morphology remained largely unchanged compared to that of the bare $BiVO_4$. No distinctive aggregation or structural distortion was observed, suggesting that the $NiFeO_x$ layer was uniformly deposited on the $BiVO_4$ surface. Energy-dispersive X-ray spectroscopy (EDS) confirmed the homogeneous distribution of Ni and Fe elements across the entire film (Fig. S2(A) in the SI), indicating uniform co-catalyst coverage without significant phase segregation.

In contrast, the $BiVO_4/NiO_x$ sample exhibited a distinct thin overlayer covering the $BiVO_4$ grains. Lower-magnification SEM images revealed the presence of microcracks on the NiO_x layer (Fig. 1(c)), which may have originated during the calcination process due to differences in thermal expansion between the oxide layers but the nano-structure has not been modified much (Fig. 1(d)). EDS analysis confirmed the coexistence and even distribution of Ni and O signals across the surface (Fig. S2(B) in the SI), confirming the formation of a continuous NiO_x layer. These surface cracks are considered to locally expose the $BiVO_4$ substrate, potentially a partial contact between $BiVO_4$ and an electrolyte solution. Although such cracks could influence local electrolyte access or interfacial electric fields, they are below the spatial resolution of the PI-PM technique and cannot be directly correlated with the observed carrier-mapping patterns. Therefore, their specific impact on the charge-carrier dynamics cannot be discussed within the present optical framework. In general, the morphology of Ni-based catalysts depends on the synthetic methods and preparation conditions,[37,38] but $NiFeO_x$ and NiO_x exhibit different surface morphologies under similar preparation conditions.

The photoelectrochemical (PEC) characteristics of the $BiVO_4$-based photoanodes (3 samples for each type) were evaluated under AM 1.5G illumination, as shown in Fig. 2. Comparing the average values, the bare $BiVO_4$ electrode exhibited an anodic photocurrent density of 0.82 mA cm^{-2} at 1.23 V *vs.* RHE, which was significantly enhanced to 1.41 and 1.98 mA cm^{-2} by the deposition of $NiFeO_x$ and NiO_x co-catalysts, respectively. These enhancements correspond to 1.7- and 2.4-fold increases relative to the pristine $BiVO_4$ sample, confirming that both co-catalysts effectively improve the water oxidation processes.

To clarify the origin of the enhanced PEC activity, the charge separation efficiency (η_{sep}) within the $BiVO_4$ bulk and the charge injection efficiency (η_{inj}) at the photoanode–electrolyte interface were quantitatively evaluated (Fig. 3). These parameters were obtained from photocurrent measurements in the presence and absence of a hole scavenger and the theoretical maximum value. The bare $BiVO_4$ exhibited limited efficiencies, with η_{sep} and η_{inj} of 40.6% and 27.0%, respectively, indicating that both bulk recombination and surface oxidation reactions restricted the overall photoresponse.

After modification with $NiFeO_x$ and NiO_x, the η_{inj} values increased markedly to 55.0% and 71.4%, while η_{sep} showed only slight variation (34.3% and 37.1%, respectively). Although the change in η_{sep} is smaller than that observed for η_{inj}, it exceeds experimental uncertainty and suggests that cocatalyst deposition may influence near-surface charge separation processes. Such effects could arise from the modifications of surface band bending, interfacial electric fields, or suppression of surface recombination. Nevertheless, the substantially larger

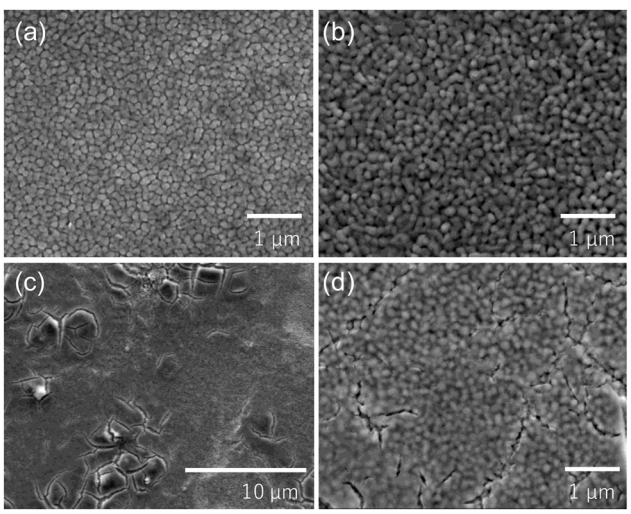

Fig. 2 SEM images of (a) bare $BiVO_4$, (b) $BiVO_4/NiFeO_x$, and (c and d) $BiVO_4/NiO_x$ photoanodes.

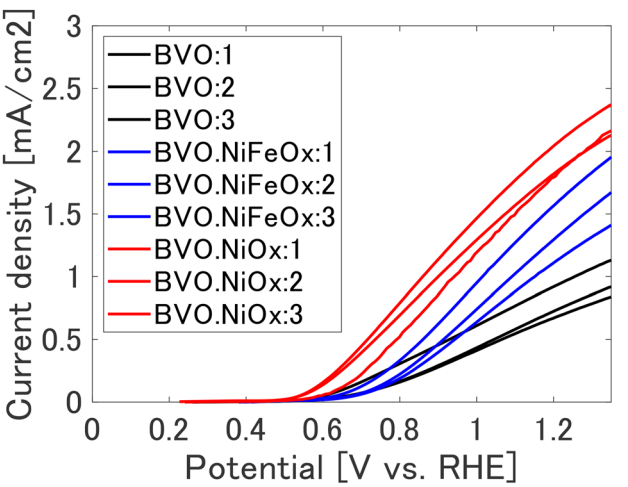

Sample	Average [mA/cm²]
Bare $BiVO_4$	0.82
$BiVO_4$ / NiFeOx	1.41
$BiVO_4$ / NiOx	1.98

Fig. 3 Linear sweep voltammograms (LSVs) of bare $BiVO_4$, $BiVO_4/NiFeO_x$, and $BiVO_4/NiO_x$ photoanodes measured under AM 1.5 G illumination (100 mW cm^{-2}) in 0.1 M phosphate buffer (pH 7.2).

enhancement in η_{inj} indicates that improved interfacial hole transfer remains the dominant factor governing the photocurrent increase. This interpretation is consistent with previous reports on metal–oxide cocatalyst modification of $BiVO_4$, where acceleration of surface reaction kinetics plays a more significant role than changes in bulk charge transport.[10–18]

Among the two cocatalysts, NiO_x produced the highest η_{inj} and the largest increase in photocurrent. This can be ascribed to its favorable band alignment with $BiVO_4$ and high intrinsic hole conductivity, which together facilitate efficient hole extraction and water-oxidation catalysis. The improved η_{inj} correlates well with the onset-potential cathodic shift observed in the PEC curves (Fig. 2), confirming that NiO_x provides superior interfacial energetics and charge-transfer pathways.

Under AM 1.5G illumination in 0.1 M PBS (pH 7.2), the Nyquist responses of bare $BiVO_4$ and $BiVO_4$/$NiFeO_x$ each display a single semicircle, whereas $BiVO_4$/NiO_x clearly shows two distinct semicircles, whose radius were smaller than the ones for the former two types. Consistent with this behavior, we employed two different equivalent circuit models (Fig. 4(a) and (b)): for bare $BiVO_4$ and $BiVO_4$/$NiFeO_x$ we assumed $R_1/(R_3, C_3)$, while for $BiVO_4$/NiO_x we assumed $R_1/(R_2, C_2)/(R_3, C_3)$. Here, R_1 denotes the ohmic resistance due to the substrate/contacts, (R_3, C_3) represents the primary interfacial charge-transfer channel at the semiconductor/electrolyte boundary, where the charge transfer resistance in the bulk is typically negligible for the $BiVO_4$ anode system. An additional (R_2, C_2) term in the NiO_x case accounts for a second process that emerges after forming the NiO_x overlayer due to transport/accumulation within the $BiVO_4$–NiO_x interface. The results for bare $BiVO_4$ and $BiVO_4$/$NiFeO_x$ are consistent with the previous result,[35] while in the case of NiO_x, a double-circuit model has not been observed for $BiVO_4$.

The transition from a single to double semicircle upon NiO_x loading indicates that, beyond lowering the primary interfacial resistance, NiO_x introduces an additional kinetically distinguishable pathway. The reduced radius of the first arc together with the emergence of the second arc suggests (i) facilitated hole injection at the electrolyte interface and (ii) a concurrent NiO_x-related storage/transfer process that becomes rate-limiting at lower frequencies.

Quantitative fitting of the PEIS spectra was carried out using equivalent circuit models. The extracted R_3 values followed the order $BiVO_4$ (1085 Ω) > $BiVO_4$/$NiFeO_x$ (798 Ω) > $BiVO_4$/NiO_x (145 Ω), consistent with the PEC performance and η_{inj} trends obtained from photocurrent analysis. This reduction in R_3 demonstrates that Ni-based cocatalysts substantially improve interfacial charge transfer, with NiO_x showing the highest catalytic activity for surface oxidation.

Time-resolved image sequences of the refractive index changes upon patterned UV pump irradiation were obtained for (a) bare $BiVO_4$, (b) $BiVO_4$/$NiFeO_x$, and (c) $BiVO_4$/NiO_x using the PI-PM method in acetonitrile (ACN), and shown in Fig. 5. The pump pattern is shown schematically at the bottom of each panel, and the analyzed regions are indicated by red rectangles. Upon excitation, a distinct contrast change corresponding to the refractive index modulation increased within 100 ns and decayed within 100 μs for all samples. The observed optical phase change arises from the locally generated photoinduced charge carriers at the semiconductor–electrolyte interface. There were no clear differences of the PI-PM image sequences observed for different types of the samples.

The local charge carrier dynamics of bare $BiVO_4$ were analyzed by clustering the pixel-by-pixel temporal responses obtained from the PI-PM image sequence in ACN (Fig. 6 for

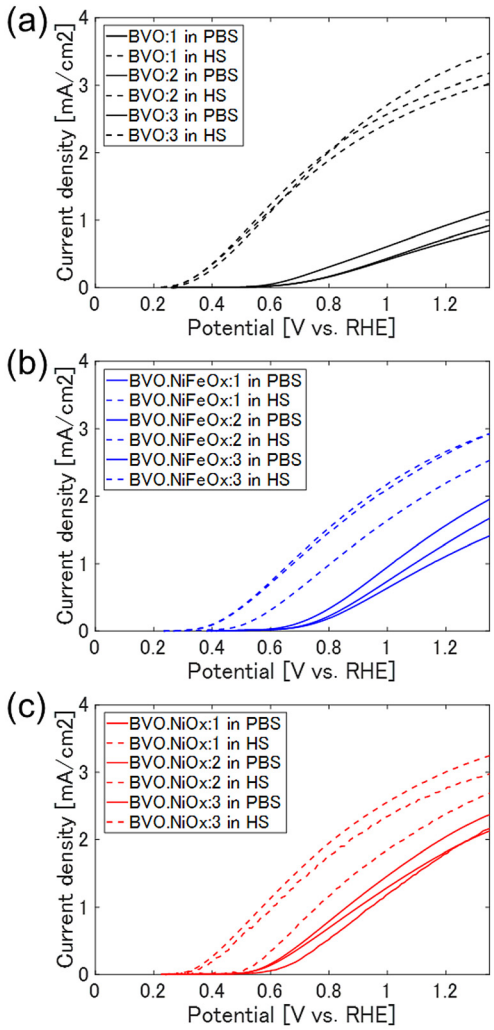

Sample	In PBS [mA/cm²]	In HS [mA/cm²]	Sep [%]	Inj [%]
Bare $BiVO_4$	0.82	3.05	40.6	27.0
$BiVO_4$ / NiFeOx	1.41	2.57	34.3	55.0
$BiVO_4$ / NiOx	1.98	2.78	37.1	71.4

Fig. 4 Charge separation (η_{sep}) and charge injection (η_{inj}) efficiencies of (a) bare $BiVO_4$, (b) $BiVO_4$/$NiFeO_x$, and (c) $BiVO_4$/NiO_x photoanodes determined from photocurrent measurements with and without a hole scavenger (HS). The measurements were carried out in a 0.1 M phosphate buffer solution (PBS, pH 7.2) under AM 1.5 G illumination. The HS corresponds to the addition of 0.1 M Na_2SO_3 aqueous solution, which suppresses surface recombination by scavenging photogenerated holes.

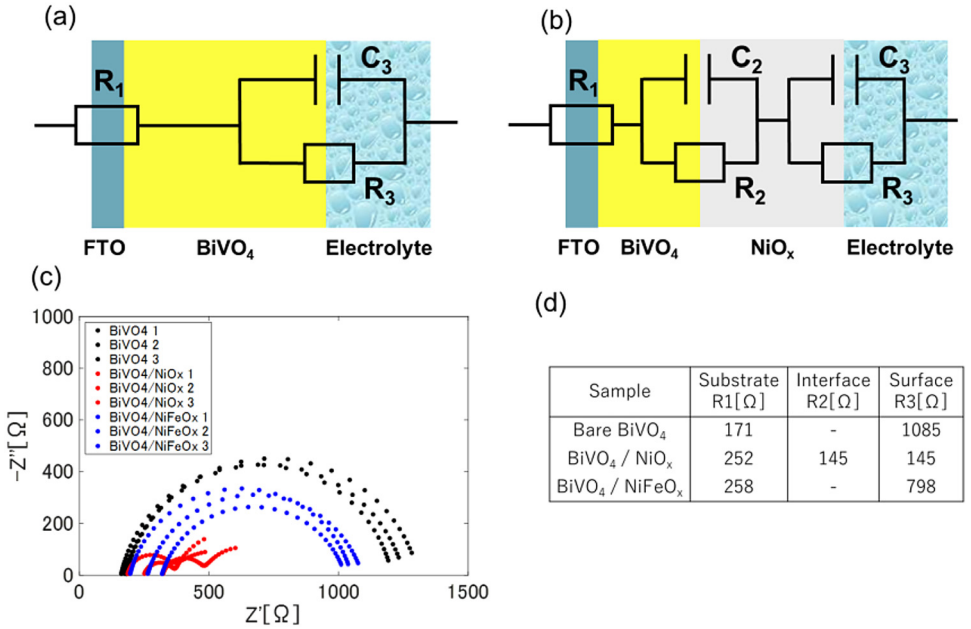

Sample	Substrate R1[Ω]	Interface R2[Ω]	Surface R3[Ω]
Bare $BiVO_4$	171	-	1085
$BiVO_4$ / NiO_x	252	145	145
$BiVO_4$ / $NiFeO_x$	258	-	798

Fig. 5 (a) Equivalent circuit used for bare $BiVO_4$ and $BiVO_4/NiFeO_x$: $R_1/(R_3, C_3)$. (b) Equivalent circuit used for $BiVO_4/NiO_x$: $R_1/(R_2,C_2)/(R_3,C_3)$. (c) Nyquist plots for bare $BiVO_4$ (black), $BiVO_4/NiFeO_x$ (blue), and $BiVO_4/NiO_x$ (red) measured under AM 1.5 G illumination in 0.1 M phosphate buffer solution (PBS, pH 7.2); 1.23 V referenced to the RHE. (d) Averaged resistance values extracted from the circuit-model based fitting.

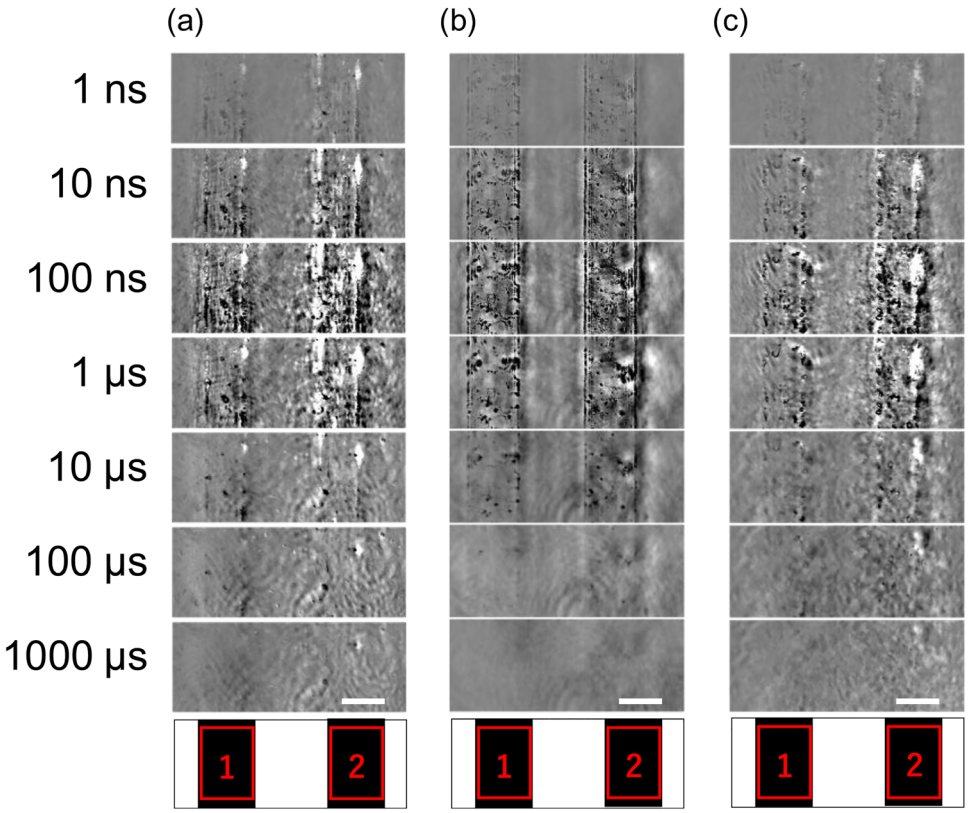

Fig. 6 Time-resolved phase image sequences of (a) bare $BiVO_4$, (b) $BiVO_4/NiFeO_x$, and (c) $BiVO_4/NiO_x$ photoanodes obtained using pattern-illumination time-resolved phase microscopy (PI-PM) under pulsed UV excitation in acetonitrile (ACN). The intensity contrast represents the refractive index change (Δn) induced by photo-excitation, corresponding to the distribution of photo-generated charge carriers. The excitation pattern is shown schematically at the bottom of each panel, and the analyzed regions are highlighted by red rectangles.

region 1 and Fig. S3 in the SI for region 2). Two representative categories of dynamics were identified within the field of view corresponding to the regions marked in Fig. 5(a). One type exhibited a single rise-and-decay response (red) with a rise time of 12 ± 1 ns and a decay time of 0.8 ± 0.1 μs, whereas the other showed a single valley-and-recovery response (blue) with a fall time of 31 ± 2 ns and a recovery time of 1.0 ± 0.1 μs. Areas showing no measurable phase change were mapped in black.

Upon introducing the hole scavenger ethanol (EtOH) as a liquid phase, the red-colored response diminished, while the blue component remained, indicating that the positive (red) response corresponds to surface-trapped holes scavenged by EtOH. Conversely, the addition of nitrobenzene (NB) as an electron scavenger suppressed the blue signal, identifying the negative (blue) response as originating from electrons. The second region showed a similar tendency as the first region. These assignments are consistent with previous PI-PM investigations of TiO_2 and $BiVO_4$ particulate systems, where the sign of the refractive index changes due to trapped electron- and hole-related processes.[26,28] The coexistence of both carrier types within the same microscopic field demonstrates the intrinsic spatial inhomogeneity of photo-excited carrier dynamics in $BiVO_4$. Such inhomogeneity, linked to variations in the surface defect density and crystallographic orientation, contributes to the moderate charge-injection efficiency and recombination loss observed in the PEC measurements.

The local charge carrier dynamics of the $BiVO_4/NiFeO_x$ sample were examined using PI-PM and the clustering analysis for two representative regions marked in Fig. 5(b). One example is shown in Fig. 7, while the other is provided in Fig. S4 in the SI. In ACN, compared with the bare $BiVO_4$, the photo-induced responses were further separated into four distinct categories. Two types of rise-and-decay responses (red and cyan) were observed with rise and decay time constants of 16 ± 1 ns/0.4 ± 0.2 μs and 52 ± 3 ns/1.5 ± 0.1 μs, respectively, and two types of valley-and-recovery responses (blue and green) with fall and recovery time constants of 16 ± 1 ns/0.5 ± 0.1 μs and 23 ± 2 ns/1.9 ± 0.1 μs, respectively. The remaining regions showing no measurable change are indicated in black.

Introduction of the hole scavenger (EtOH) selectively diminished only the slower positive (cyan) response, while the faster red response remained unchanged. This behavior suggests that the cyan component corresponds to reactive surface-trapped holes capable of oxidation, whereas the red component represents nonreactive or deeply trapped holes with limited oxidative activity. Conversely, upon addition of the electron scavenger (NB), only the slower negative (green) response decreased, confirming its assignment to reactive trapped electrons, while the faster blue response was unaffected. The second region shows an almost similar tendency to that of the first region. These findings indicate that the deposition of $NiFeO_x$ introduces energetically distinct cocatalyst states that selectively capture photogenerated holes, prolonging their lifetime and enhancing their oxidative potential. The emergence of the slow electron response (green) further implies that electron–hole recombination pathways are partially suppressed, extending electron lifetime through secondary trapping processes. The separation of both hole and electron responses into fast (non-reactive) and slow (reactive) components clearly demonstrates the role of $NiFeO_x$ in moderating charge recombination and stabilizing interfacial or near-surface accumulated reactive charge carriers participating in solution-phase reactions. In this work, ''reactive'' carriers are defined operationally as those whose PI-PM temporal responses are selectively altered by the

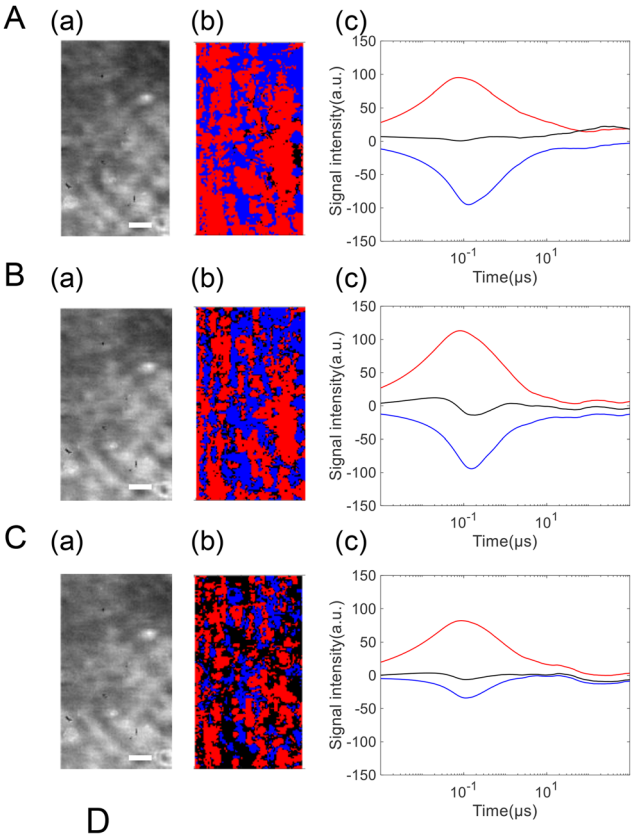

Solvent	Category	Ratio [%]	Rise [ns]	Decay [μs]
ACN	1 (Red)	60	12 ± 1	0.8 ± 0.1
	3 (Blue)	37	31 ± 2	1.0 ± 0.1
	5 (Black)	3	-	-
EtOH	1 (Red)	45	12 ± 1	0.7 ± 0.1
	3 (Blue)	38	39 ± 3	0.8 ± 0.1
	5 (Black)	17	-	-
NB/ EtOH	1 (Red)	36	12 ± 1	0.8 ± 0.1
	3 (Blue)	18	36 ± 3	0.4 ± 0.1
	5 (Black)	46	-	-

Fig. 7 The clustering analyses of the charge carrier responses of a bare $BiVO_4$ in (A) ACN, (B) EtOH, and (C) NB/EtOH in region 1 in Fig. 5(a) correspond to a microscopic image, and the corresponding categorized map is shown in (b), and the scale bar corresponds to 10 μm. The averaged responses for the categorized responses are shown in (c). The area ratios of categories and the rise/decay times for the categories are shown in (d).

introduction of electron or hole scavengers, indicating their participation in interfacial redox reactions. While PI-PM does not directly prove involvement in water oxidation, the correlation of these carrier populations with enhanced η_{inj}, reduced interfacial resistance, and improved PEC performance supports their functional relevance to the oxygen-evolution process.

It should be noted that PI-PM detects refractive index changes integrated along the optical path of the probe beam, and its depth resolution is limited by the diffraction-limited confocal parameter of the microscope (a few micron) rather than the optical penetration depth of the pump light. Therefore, nanometer-scale distinction among carriers located within $BiVO_4$, within the cocatalyst overlayer, or exactly at the $BiVO_4$–cocatalyst interface is not directly accessible.

However, the identification of the slow cyan and green components as reactive carriers is supported by their selective suppression in the presence of scavengers. Because scavenger reactions occur at the solid–liquid interface, the affected charge carriers must be located at, or able to reach, the solution interface. Thus, these components are attributed to interfacial or near-surface accumulated charge carriers participating in solution-phase reactions.

Finally, the PI-PM analysis for the $BiVO_4/NiO_x$ photoanode revealed further evolution of the microscopic charge carrier behavior compared with $BiVO_4$ and $BiVO_4/NiFeO_x$ (Fig. 8). Two representative regions indicated in Fig. 5(c) were analyzed; one of them is shown here, and the other in Fig. S5 in the SI. Similarly to the $NiFeO_x$ case, both the hole- and electron-related responses were separated into two components, giving four distinct categories. Two rise-and-decay responses were identified with the rise and decay time constants of 17 ± 1 ns/0.4 ± 0.1 μs (red) and 25 ± 2 ns/1.7 ± 0.1 μs (cyan), and two valley-and-recovery responses with the fall and recovery constants of 14 ± 1 ns/0.3 ± 0.1 μs (blue) and 25 ± 2 ns/3.2 ± 0.2 μs (green). Regions without the measurable phase change were mapped in black.

The scavenger effects were consistent with those observed for $BiVO_4/NiFeO_x$: the slower positive (cyan) and slower negative (green) components were selectively suppressed by EtOH (hole scavenger) and NB (electron scavenger), respectively. The second region also showed a similar tendency. This confirms their assignment as reactive trapped holes and reactive trapped electrons, while the faster (red and blue) components correspond to non-reactive or rapidly recombining carriers.

Compared with the $NiFeO_x$ case, the spatial fraction of the reactive carrier regions increased markedly: reactive holes from 19 → 33% and reactive electrons from 18 → 33%. Moreover, the lifetimes of the reactive carriers were extended: holes from 1.5 → 1.7 μs and electrons from 1.9 → 3.2 μs. These results indicate that the NiO_x overlayer not only enhances charge separation but also prolongs carrier survival, thereby improving the overall reaction efficiency. The enhanced stabilization of both reactive holes and electrons implies that NiO_x provides superior interfacial energetics and catalytic activity, consistent with the highest η_{inj} and PEC performance observed among the samples (Fig. 9).

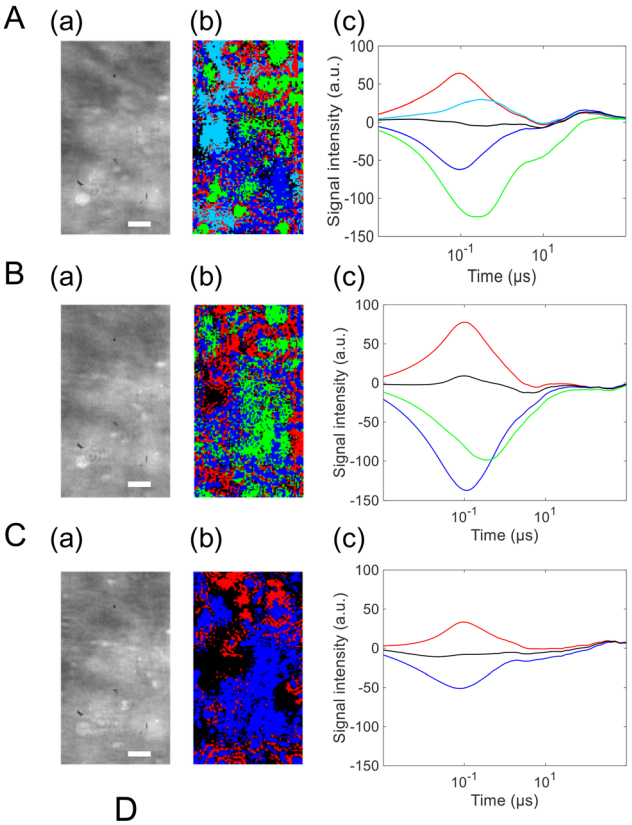

Solvent	Category	Ratio [%]	Rise [ns]	Decay [μs]
ACN	1 (Red)	20	16 ± 1	0.4 ± 0.2
	2 (Cyan)	19	52 ± 3	1.5 ± 0.1
	3 (Blue)	30	16 ± 1	0.5 ± 0.1
	4 (Green)	18	23 ± 2	1.9 ± 0.1
	5 (Black)	13	-	-
EtOH	1 (Red)	23	19 ± 1	0.5 ± 0.1
	2 (Cyan)	0	-	-
	3 (Blue)	33	14 ± 1	0.7 ± 0.1
	4 (Green)	27	27 ± 1	2.5 ± 0.1
	5 (Black)	16	-	-
NB/EtOH	1 (Red)	14	26 ± 1	0.4 ± 0.1
	2 (Cyan)	0	-	-
	3 (Blue)	42	9 ± 1	0.5 ± 0.1
	4 (Green)	0	-	-
	5 (Black)	44	-	-

Fig. 8 Clustering analyses of the charge carrier responses of the $BiVO_4/NiFeO_x$ photoanode in (A) ACN, (B) EtOH, and (C) NB/EtOH in region 1 in Fig. 5(b) correspond to a microscopic image, and the corresponding categorized map is shown in (b), and the scale bar corresponds to 10 μm. The averaged responses for the categorized responses are shown in (c). The ratios of the categories and the rise/decay times for the categories are shown in (d).

Discussion

To facilitate a unified comparison of the functional parameters extracted from PEC, PEIS, and PI-PM analyses, the key quantitative metrics are summarized in Table 1. This table highlights the systematic differences in the charge-injection efficiency,

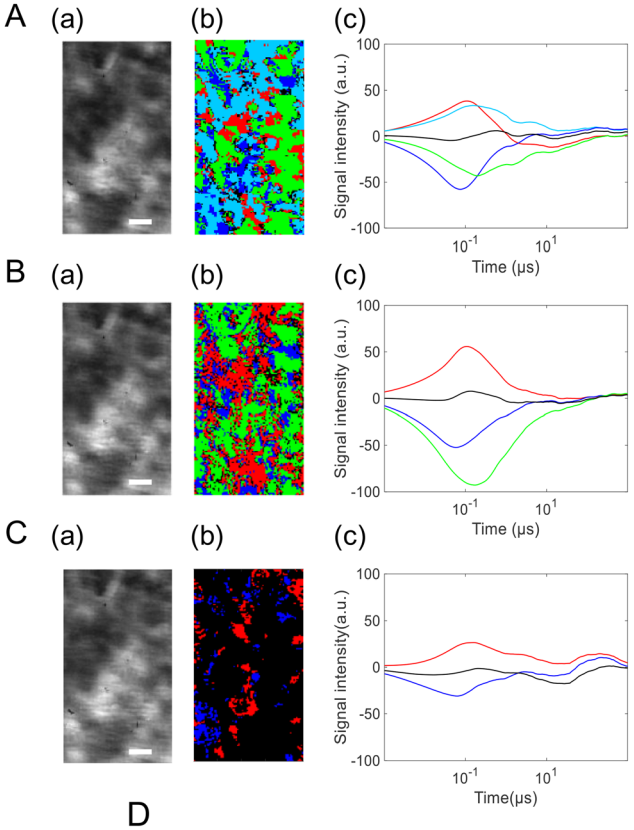

D

Solvent	Category	Ratio [%]	Rise [ns]	Decay [μs]
ACN	1 (Red)	13	17 ± 1	0.4 ± 0.1
	2 (Cyan)	33	25 ± 2	1.7 ± 0.1
	3 (Blue)	12	14 ± 1	0.3 ± 0.1
	4 (Green)	33	25 ± 2	3.2 ± 0.2
	5 (Black)	8	-	-
EtOH	1 (Red)	28	24 ± 1	0.5 ± 0.1
	2 (Cyan)	0	-	-
	3 (Blue)	17	10 ± 1	0.4 ± 0.1
	4 (Green)	41	17 ± 1	1.4 ± 0.1
	5 (Black)	14	-	-
NB/EtOH	1 (Red)	8	27 ± 2	1.6 ± 0.2
	2 (Cyan)	0	-	-
	3 (Blue)	6	8 ± 1	0.2 ± 0.1
	4 (Green)	0	-	-
	5 (Black)	86	-	-

Fig. 9 Clustering analyses of the charge carrier responses of the $BiVO_4$/NiO_x photoanode in (A) ACN, (B) EtOH, and (C) NB/EtOH in region 2 in Fig. 5(c) correspond to a microscopic image, and the corresponding categorized map is shown in (b), and the scale bar corresponds to 10 μm. The averaged responses for the categorized responses are shown in (c). The ratios of the categories and the rise/decay times for the categories are shown in (d).

separation efficiency, carrier lifetime, and spatial fraction of reactive domains among the bare, $NiFeO_x$-, and NiO_x-modified $BiVO_4$ photoanodes. The combined results from SEM, PEC, η_{sep}/η_{inj} analysis, and PI-PM measurements provide a consistent picture of how the Ni-based cocatalysts modulate charge separation and transfer in $BiVO_4$ photoanodes. The SEM observations confirmed that both $NiFeO_x$ and NiO_x form continuous overlayers on the $BiVO_4$ surfaces while maintaining the underlying grain structure, suggesting that the differences in activity arise primarily from electronic and interfacial, rather than morphological variations. The PEC and efficiency analyses reveal that deposition of Ni-based oxides predominantly enhances the charge-injection efficiency (η_{inj}), while η_{sep} exhibits only moderate variation. Although cocatalyst loading may influence near-surface separation processes through the modifications of band bending or surface recombination, the substantially larger increase in η_{inj} indicates that acceleration of interfacial hole transfer is the primary factor governing the performance enhancement. This trend is consistent with previous studies of metal-oxide-modified $BiVO_4$ systems.[12] The improvement is most pronounced for NiO_x, consistent with its higher photocurrent (PEC) and lower charge-transfer resistance in PEIS.

The PI-PM results provide microscopic insight into these macroscopic behaviors. In $BiVO_4$/$NiFeO_x$, the cocatalyst introduces micron-scale active sites, generating spatially separated fast (nonreactive) and slow (reactive) hole/electron components. In this work, "reactive" carriers are defined operationally as those whose PI-PM temporal responses are selectively altered by the introduction of electron or hole scavengers, indicating their participation in interfacial redox reactions. While PI-PM does not directly prove involvement in water oxidation, the correlation of these carrier populations with enhanced η_{inj}, reduced interfacial resistance, and improved PEC performance supports their functional relevance to the oxygen-evolution process. The slower components (cyan and green) represent reactive trapped carriers that participate in surface redox reactions, whose distribution reflects the localized activity of the cocatalyst, even though they were homogeneously coated. In $BiVO_4$/NiO_x, a similar spatial distribution is observed, but the proportion of reactive regions increases (holes 19 → 33% and electrons 18 → 33%) and both the hole and electron lifetimes are further prolonged (holes 1.7 μs and electrons 3.2 μs). These changes signify more effective charge separation and stabilization at the NiO_x interface. In the present work, the terms "localized" and "uniform" are defined operationally based on the spatial fraction and distribution of the reactive carrier pixels in the PI-PM categorization maps rather than on geometrical domain size analysis. Thus, "localized" refers to a smaller reactive area fraction with spatial discontinuity, whereas "uniform" indicates a larger and more spatially continuous reactive fraction.

The appearance of a second semicircle in the PEIS spectra for $BiVO_4$/NiO_x supports the presence of an additional slower charge transfer pathway, corresponding to the interfacial charge accumulation or transport within the $BiVO_4$/NiO_x junction, in agreement with the charge carrier dynamics observed in PI-PM. Overall, the synergistic interpretation of PEC, PEIS, and PI-PM results demonstrates that NiO_x achieves the most efficient interfacial charge separation and transfer by stabilizing reactive holes and facilitating hole-driven oxidation while minimizing surface recombination losses.

Table 1 Summary of key quantitative parameters extracted from PEC, PEIS, and PI-PM analyses for bare, $NiFeO_x$-, and NiO_x-modified $BiVO_4$ photoanodes. Reported values include the photocurrent density at 1.23 V *vs.* RHE, charge-injection efficiency (η_{inj}), charge-separation efficiency (η_{sep}), reactive carrier lifetimes determined from PI-PM categorization, and spatial fractions of the reactive carrier regions

Sample	PEC [mA cm^{-2}]	Scavenger analysis		PI-PM measurement			
		Separation [%]	Injection [%]	Category	Ratio [%]	Rise [ns]	Decay [μs]
Bare $BiVO_4$	0.82	40.6	27.0	Holes	60	12 ± 1	0.8 ± 0.1
				Electrons	37	31 ± 2	1.0 ± 0.1
				No response	3	—	—
$BiVO_4$/NiFeOx	1.41	34.3	55.0	Holes	20	16 ± 1	0.4 ± 0.2
				Reactive holes	19	52 ± 3	1.5 ± 0.1
				Electrons	30	16 ± 1	0.5 ± 0.1
				Reactive electrons	18	23 ± 2	1.9 ± 0.1
				No response	13	—	—
$BiVO_4$/NiOx	1.98	37.1	71.4	Electrons	13	17 ± 1	0.4 ± 0.1
				Reactive electrons	33	25 ± 2	1.7 ± 0.1
				Holes	12	14 ± 1	0.3 ± 0.1
				Reactive holes	33	25 ± 2	3.2 ± 0.2
				No response	8	—	—

The improvements observed for both $NiFeO_x$- and NiO_x-modified $BiVO_4$ photoanodes in this study can be rationalized by considering previous work on their interfacial roles, catalytic characteristics, and electronic interactions with $BiVO_4$. $NiFeO_x$ has long been recognized as one of the most active oxygen-evolution cocatalysts for $BiVO_4$, owing to its Fe-mediated enhancement of NiOOH redox activity, its capacity for dynamic hole storage, and its ability to suppress surface recombination.[12–14] The mechanistic picture in which NiFeOx accelerates the OER through rapid hole capture into Fe-tuned NiOOH motifs and stabilizes the semiconductor surface by mitigating recombination pathways.

NiO*x*, although chemically simpler, has been demonstrated to provide a different but complementary set of functionalities, including the p–n junction formation and an increase in surface band bending in $BiVO_4$.[17,18] Also, it is indicated that NiO*x* serves not only as a hole-extraction overlayer but also as a tunable electronic scaffold capable of passivating deep traps and facilitating efficient hole transfer to the electrolyte.[15,16] Across these studies, NiO*x* is shown to improve $BiVO_4$ performance by forming favorable interfacial band alignment, suppressing recombination through surface passivation, and enabling faster OER kinetics.

Although SEM–EDS analysis indicates homogeneous cocatalyst coverage, the PI-PM maps reveal spatially heterogeneous reactive domains, particularly in the $NiFeO_x$ case. Such functional inhomogeneity despite uniform structural coverage has been frequently observed in our previous cocatalyst mapping studies[27,28,39] and reflects spatial variation in charge accumulation and interfacial transfer efficiency rather than discontinuity of the cocatalyst layer itself.

The localized, long-lived hole-accumulation domains observed for $NiFeO_x$ are consistent with previously reported hole-storage behavior associated with Ni–Fe–OOH species in similar systems, which explains why the photocurrent (1.41 mA cm^{-2}) is enhanced yet remains below the highest reported values. However, the PI-PM and PEC measurements provide functional insight into charge accumulation and transfer dynamics rather than direct chemical-state identification. Definitive determination of the catalytic species would require complementary spectroscopic techniques such as XPS, XANES, or operando Raman spectroscopy. In contrast, NiO_x forms a more uniform interfacial extraction layer, generating broader regions of slow-decay, hole-reactive signals in the PI-PM maps. Likewise, the broader spatial distribution and enhanced carrier stabilization observed for NiO_x are consistent with literature reports suggesting favorable band alignment or p–n junction–like interfacial energetics.[17,18] Further confirmation of the electronic-structure characterization is needed to support this interpretation.

Conclusion

In this study, we systematically investigated the effects of $NiFeO_x$ and NiO_x cocatalysts on $BiVO_4$ photoanodes using a combination of PEC characterization, impedance analysis, and patterned-illumination time-resolved phase microscopy (PI-PM). Both cocatalysts significantly enhanced the photocurrent and charge-injection efficiency (η_{inj}), confirming their essential roles in accelerating interfacial water-oxidation kinetics. However, the origin of these improvements differs between the two systems. $NiFeO_x$ increased η_{inj} to 55.0% and improved photocurrent through the formation of localized, catalytically active domains that stabilize reactive holes. In contrast, NiO_x led to a higher η_{inj} of 71.4% and achieved the largest photocurrent (1.98 mA cm^{-2}), consistent with its ability to form a uniform interfacial extraction layer with favorable band alignment and effective surface passivation.

The PI-PM imaging revealed critical microscopic distinctions underlying these macroscopic enhancements. $NiFeO_x$ produced spatially discrete slow-decay carrier regions corresponding to reactive trapped holes and electrons, indicating that a fraction of the cocatalyst surface operates as active catalytic sites. NiO_x, on the other hand, generated a broader distribution of reactive domains with prolonged carrier lifetimes, reflecting more efficient interfacial charge stabilization and a more continuous hole-extraction pathway. These PI-PM results provide the first direct visualization of how $NiFeO_x$ and NiO_x modulate

surface carrier populations differently. This insight not only explains the differing performance outcomes observed in this work but also provides design principles for future cocatalyst engineering—namely, optimizing both domain uniformity (as in NiO_x) and catalytic site activity (as in $NiFeO_x$) to approach the intrinsic limits of $BiVO_4$-based photoanodes.

Beyond demonstrating the enhanced performance of Ni-based cocatalysts, this study establishes a quantitative link between spatially resolved carrier dynamics and macroscopic injection efficiency. By directly comparing $NiFeO_x$ and NiO_x under identical conditions, we reveal that spatial continuity and stabilization of reactive carrier domains are key determinants of interfacial charge-transfer efficiency. This comparative framework highlights the utility of PI-PM as a functional diagnostic tool for rational cocatalyst design.

Author contributions

YN performed the experiments and analyses, HN supported the preparation of samples and KK guided the overall research. YN and KK wrote the manuscript and all the authors reviewed it.

Conflicts of interest

The authors declare that they have no competing interests or other interests that might be perceived to influence the results and/or discussion reported in this article.

Data availability

All data supporting the findings of this study are available within the article and its supplementary information (SI). Supplementary information: Fig. S1: PI-PM optical setup. Fig. S2: EDS results for $BiVO_4/NiFeO_x$ and $BiVO_4/NiO_x$. Fig. S3: PI-PM results for $BiVO_4$ (region 2). Fig. S4: PI-PM results for $BiVO_4/NiFeO_x$ (region 2). Fig. S5: PI-PM results for $BiVO_4/NiO_x$ (region 2). See DOI: https://doi.org/10.1039/d5cp05032d.

Acknowledgements

This research was financially supported by the Institute of Science and Engineering, Chuo University, the Global - Learning & Academic Research Institution for Master's PhD students, and the Postdocs (LAMP) Program of the National Research Foundation of Korea (NRF) grant funded by the Ministry of Education (No. RS-2024-00445180).

References

1 A. Kudo, K. Omori and H. Kato, *J. Am. Chem. Soc.*, 1999, **121**, 11459–11467.
2 Y. Park, K. J. McDonald and K.-S. Choi, *Chem. Soc. Rev.*, 2013, **42**, 2321–2337.
3 C. Martinez Suarez, S. Hernández and N. Russo, *Appl. Catal., A*, 2015, **504**, 158–170.
4 M. Malathi, J. Madhavan, M. Ashokkumar and P. Arunachalam, *Appl. Catal., A*, 2018, **555**, 47–74.
5 Q. Wang and K. Domen, *Chem. Rev.*, 2020, **120**, 919–985.
6 T. Wang, K. Song, H. Liu, H. Li, Y. Zhang, W. Ren, R. Zhang, K. Li, F. He, Z. Qin and H. Hou, *Chem. Eng. J.*, 2025, **509**, 161333.
7 Z. Yuan, L. Jiang, H. Yang, Z. Liang, D. Zhang, B. Li, H. Hou, W. Yang and X. Zhan, *Small*, 2025, **21**, e06133.
8 H. Hou, G. Shao, Y. Wang, W.-Y. Wong and W. Yang, *Carbon Energy*, 2024, **6**, e373.
9 T. Liu, Z. Pan, K. Kato, J. J. M. Vequizo, R. Yanagi, X. Zheng, W. Yu, A. Yamakata, B. Chen, S. Hu, K. Katayama and C. Chu, *Nat. Commun.*, 2022, **13**, 7783.
10 X. Li, Z. Wang, A. Sasani, A. Baktash, K. Wang, H. Lu, J. You, P. Chen, P. Chen, Y. Bao, S. Zhang, G. Liu and L. Wang, *Nat. Commun.*, 2024, **15**, 9127.
11 J. Zhang, Y. Huang, X. Lu, J. Yang and Y. Tong, *ACS Sustainable Chem. Eng.*, 2021, **9**, 8306–8314.
12 B. Zhang, S. Yu, Y. Dai, X. Huang, L. Chou, G. Lu, G. Dong and Y. Bi, *Nat. Commun.*, 2021, **12**, 6969.
13 L. Fu, Z. Li, X. Shang and Y. Zheng, *J. Mater. Chem. A*, 2025, **13**, 13951–13961.
14 Y. Kuang, Q. Jia, H. Nishiyama, T. Yamada, A. Kudo and K. Domen, *Adv. Energy Mater.*, 2016, **6**, 1501645.
15 S. Wang, Z. Shi, K. Du, Z. Ren, H. Feng, J. Wang, L. Wang, D. Cui, Y. Du and W. Hao, *Small Methods*, 2025, **9**, 2401443.
16 D. A. Reddy, Y. Kim, K. A. J. Reddy, M. Gopannagari, A. P. Rangappa, D. Praveen Kumar, A. A. Sasikala Devi, D. Murali, H. S. Ahn and T. K. Kim, *ACS Appl. Energy Mater.*, 2021, **4**, 11353–11366.
17 M. Zhong, T. Hisatomi, Y. Kuang, J. Zhao, M. Liu, A. Iwase, Q. Jia, H. Nishiyama, T. Minegishi, M. Nakabayashi, N. Shibata, R. Niishiro, C. Katayama, H. Shibano, M. Katayama, A. Kudo, T. Yamada and K. Domen, *J. Am. Chem. Soc.*, 2015, **137**, 5053–5060.
18 M. Zhang, R. P. Antony, S. Y. Chiam, F. F. Abdi and L. H. Wong, *ChemSusChem*, 2019, **12**, 2022–2028.
19 I. Grigioni, K. G. Stamplecoskie, E. Selli and P. V. Kamat, *J. Phys. Chem. C*, 2015, **119**, 20792–20800.
20 J. Ravensbergen, F. F. Abdi, J. H. van Santen, R. N. Frese, B. Dam, R. van de Krol and J. T. M. Kennis, *J. Phys. Chem. C*, 2014, **118**, 27793–27800.
21 S. Selim, L. Francàs, M. García-Tecedor, S. Corby, C. Blackman, S. Gimenez, J. R. Durrant and A. Kafizas, *Chem. Sci.*, 2019, **10**, 2643–2652.
22 Y. Suzuki, D. H. K. Murthy, H. Matsuzaki, A. Furube, Q. Wang, T. Hisatomi, K. Domen and K. Seki, *J. Phys. Chem. C*, 2017, **121**, 19044–19052.
23 H. L. Tan, X. Wen, R. Amal and Y. H. Ng, *J. Phys. Chem. Lett.*, 2016, **7**, 1400–1405.
24 A. Yamakata, C. S. K. Ranasinghe, N. Hayashi, K. Kato and J. J. M. Vequizo, *ACS Appl. Energy Mater.*, 2020, **3**, 1207–1214.
25 K. Katayama, *Phys. Chem. Chem. Phys.*, 2024, **26**, 9783–9815.
26 Y. Nakatsukasa and K. Katayama, *J. Phys. Chem. C*, 2025, **129**, 18935–18945.

27 T. Chugenji, Z. Pan and K. Katayama, *J. Phys. Chem. C*, 2022, **126**, 19319–19326.
28 Y. Egawa, K. Kawaguchi, Z. Pan and K. Katayama, *J. Chem. Phys.*, 2024, **160**, 164705.
29 K. Katayama, T. Chugenji and K. Kawaguchi, *AIP Adv.*, 2021, **11**, 115215.
30 X. Huang, J. Fan, L. Li, H. Liu, R. Wu, Y. Wu, L. Wei, H. Mao, A. Lal, P. Xi, L. Tang, Y. Zhang, Y. Liu, S. Tan and L. Chen, *Nat. Biotechnol.*, 2018, **36**, 451–459.
31 U. von Luxburg, *Stat. Comput.*, 2007, **17**, 395–416.
32 K. Sayama, A. Nomura, T. Arai, T. Sugita, R. Abe, M. Yanagida, T. Oi, Y. Iwasaki, Y. Abe and H. Sugihara, *J. Phys. Chem. B*, 2006, **110**, 11352–11360.
33 K. Sayama, A. Nomura, T. Arai, T. Sugita, R. Abe, M. Yanagida, T. Oi, Y. Iwasaki, Y. Abe and H. Sugihara, *J. Phys. Chem. B*, 2006, **110**, 11352–11360.
34 S. Zhang, L. Shen, T. Ye, K. Kong, H. Ye, H. Ding, Y. Hu and J. Hua, *Energy Fuels*, 2020, **34**, 5016–5023.
35 K. Kobayashi, Y. Nagai, Z. Pan and K. Katayama, *J. Photochem. Photobiol., A*, 2023, **440**, 114651.
36 K. Katayama, Y. Takeda, K. Shimaoka, K. Yoshida, R. Shimizu, T. Ishiwata, A. Nakamura, S. Kuwahara, A. Mase, T. Sugita and M. Mori, *Analyst*, 2014, **139**, 1953–1959.
37 G. Shi, C. Arata, D. A. Tryk, T. Tano, M. Yamaguchi, A. Iiyama, M. Uchida, K. Iida, S. Watanabe and K. Kakinuma, *ACS Omega*, 2023, **8**, 13068–13077.
38 M. K. Beisembekov, G. I. Omarbekova, S. K. Tazhibayev, A. K. Aimukhanov, A. S. Baltabekov, A. Z. Ziyat and A. K. Zeinidenov, *Opt. Mater.*, 2024, **151**, 115398.
39 T. Chugenji, Z. Pan, V. Nandal, K. Seki, K. Domen and K. Katayama, *Phys. Chem. Chem. Phys.*, 2022, **24**, 17485–17495.